AGU PUBLICATIONS

Geochemistry, Geophysics, Geosystems

RESEARCH ARTICLE
10.1002/2015GC006161

Constraining mantle viscosity structure for a thermochemical mantle using the geoid observation

Xi Liu[1] and Shijie Zhong[1]

[1]Department of Physics, University of Colorado at Boulder, Boulder, Colorado, USA

Key Points:
- Thermochemical mantle models with dense LLSVPs well reproduce the observed geoid
- Inferred mantle viscosity structures are similar for thermochemical and whole mantle models
- A larger conversion factor is required to fit the geoid in thermochemical mantle models

Correspondence to:
X. Liu,
Xi.Liu@colorado.edu

Citation:
Liu, X., and S. Zhong (2016), Constraining mantle viscosity structure for a thermochemical mantle using the geoid observation, *Geochem. Geophys. Geosyst.*, *17*, 895–913, doi:10.1002/2015GC006161.

Received 30 OCT 2015
Accepted 26 JAN 2016
Accepted article online 2 FEB 2016
Published online 15 MAR 2016

Abstract Long-wavelength geoid anomalies provide important constraints on mantle dynamics and viscosity structure. Previous studies have successfully reproduced the observed geoid using seismically inferred buoyancy in whole-mantle convection models. However, it has been suggested that large low shear velocity provinces (LLSVPs) underneath Pacific and Africa in the lower mantle are chemically distinct and are likely denser than the ambient mantle. We formulate instantaneous flow models based on seismic tomographic models to compute the geoid and constrain mantle viscosity by assuming both thermochemical and whole-mantle convection. Geoid modeling for the thermochemical model is performed by considering the compensation effect of dense thermochemical piles and removing buoyancy structure of the compensation layer in the lower mantle. Thermochemical models well reproduce the observed geoid, thus reconciling the geoid with the interpretation of LLSVPs as dense thermochemical piles. The viscosity structure inverted for thermochemical models is nearly identical to that of whole-mantle models. In the preferred model, the lower mantle viscosity is ~10 times higher than the upper mantle viscosity that is ~10 times higher than the transition zone viscosity. The weak transition zone is consistent with the proposed high water content there. The geoid in thermochemical mantle models is sensitive to seismic structure at mid-mantle depths, suggesting a need to improve seismic imaging resolution there. The geoid modeling constrains the vertical extent of dense and stable chemical piles to be within ~500 km above CMB. Our results have implications for mineral physics, seismic tomographic studies, and mantle convection modeling.

1. Introduction

The geoid modeling using instantaneous mantle flow models based on seismic velocity anomalies can provide a critical constraint on the mantle rheology and buoyancy structure. Classic studies using this approach and assuming a whole-mantle, purely thermal convection model [e.g., *Hager and Richards*, 1989; *Ricard et al*., 1993; *King and Masters*, 1992; *King*, 1995; *Mitrovica and Forte*, 2004; *Ghosh et al*., 2010] have estimated that the viscosity in the lower mantle is about 30–60 times higher than that in the upper mantle. However, those models may have been over-simplified, because the large-scale lower mantle structures exhibit complex seismic characteristics which may imply compositional heterogeneities [e.g., *Su and Dziewonski*, 1997; *Masters et al*., 2000; *Wen et al*., 2001; *Ni et al*., 2002; *He and Wen*, 2009]. For example, the large low shear velocity provinces (LLSVPs) in the lower mantle (Figure 1a) have been proposed as chemically distinct and stable piles [e.g., *Wen et al*., 2001; *Ni et al*., 2002] that help reconcile both seismic and geochemical observations [e.g., *Hofmann*, 1997; *Kellogg et al*., 1999; *Kunz et al*., 1998; *Boyet and Carlson*, 2005; *Jackson et al*., 2014], although some studies suggest that the LLSVPs have a purely thermal origin [e.g., *Davies et al*., 2012]. Chemical piles alter the lowermost mantle buoyancy structure and have been found to influence the mantle dynamics [e.g., *Tackley*, 1998; *Kellogg et al*., 1999; *Davaille*, 1999; *McNamara and Zhong*, 2005; *Zhang et al*., 2010] as well as their surface manifestation such as the geoid and dynamic topography [*Liu and Zhong*, 2015]. Thus, it is necessary to reexamine the geoid modeling and its constraint on mantle viscosity considering the effects of the thermochemical mantle convection based on seismic tomographic models.

Constructing buoyancy structure from the seismic tomographic models in those chemically heterogeneous regions is difficult due to the mixture of both thermal and compositional effects, and uncertainties in seismic, compositional and mineral physics mantle models. In their geoid modeling study, *Steinberger and Torsvik* [2010] simply removed the buoyancy structure of the thermochemical layer (i.e., bottom 300 km of the mantle). Another geoid modeling study considering possible chemical effects on mantle buoyancy

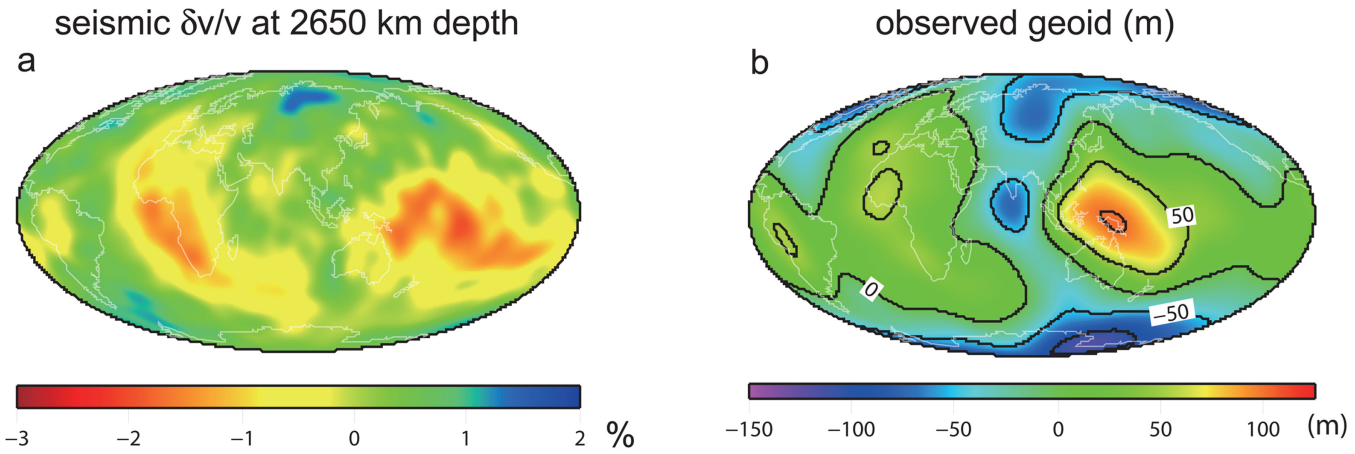

Figure 1. (a) Seismic shear wave speed anomaly δv/v (model SAW642ANb) at 2650 km depth, and (b) the observed geoid at degrees 2–12. Contours of 50 m are plotted in Figure 1b.

suggested that the LLSVPs would be overall buoyant in order to fit the geoid [*Forte and Mitrovica*, 2001], thus raising the question whether the LLSVPs represent stable thermochemical structures over long time scales. In time-dependent, dynamically self-consistent thermochemical mantle convection models, *Liu and Zhong* [2015] found that the general characteristics of the surface geoid and dynamic topography over stable dense thermochemical piles, after reaching a dynamic equilibrium, resemble the observations. Additionally, *Liu and Zhong* [2015] showed that dense thermochemical piles have a compensation effect on the geoid such that the bottom ∼1000 km of the mantle (i.e., a compensation layer), or 2–3 times of the maximum thickness of the chemical piles, has a zero net contribution to the geoid at long wavelengths. The compensation effect occurs because the geoid anomalies from negatively buoyant chemical piles are offset by those from hot and buoyant normal mantle above the piles. Considering the compensation effect, the geoid modeling for the thermochemical model with stable chemical piles can be done following the same approach as that for whole mantle models [e.g., *Hager and Richards*, 1989] except that the mantle buoyancy structure in the compensation layer, including the LLSVPs, needs to be removed. The mantle above the compensation layer can be seen as isochemical with buoyancy structure that can be determined from seismic tomographic models with a conversion factor [e.g., *Hager and Richards*, 1989; *Forte and Mitrovica*, 2001; *Ghosh et al*., 2010].

This study investigates how well the geoid can be explained in instantaneous flow models in which mantle buoyancy structure is derived from seismic tomographic models considering the compensation effect for the thermochemical mantle as reported in *Liu and Zhong* [2015]. This study also reexamines the geoid constraints on mantle viscosity structure for a thermochemical mantle and compares the inverted mantle viscosity with that inferred from previous purely thermal mantle models. The paper is organized as follows. Next section describes the model formulation and procedures, section 3 presents results, and sections 4 and 5 are for discussion and conclusion.

2. Models and Procedures

2.1. Geoid Modeling

The instantaneous flow models are formulated in a 3-D spherical geometry. Assuming an incompressible fluid and constant thermodynamic parameters except for the viscosity, the governing equations for the conservation laws of the mass and momentum are:

$$\nabla \cdot \boldsymbol{u} = 0, \tag{1}$$

$$-\nabla p + \nabla \cdot \left[\eta\left(\nabla \boldsymbol{u} + \nabla^T \boldsymbol{u}\right)\right] - \delta\rho g \boldsymbol{e}_r = 0, \tag{2}$$

where $\boldsymbol{u}$ is the velocity vector, p is the dynamic pressure, η is the viscosity, g is the gravitational acceleration, and $\delta\rho$ is the density anomaly.

The density anomaly $\delta\rho$ in equation (2) is determined from seismically observed relative shear-velocity anomaly $\frac{\delta v_s}{v_s}$ by:

$$\frac{\delta\rho}{\rho}=c\frac{\delta v_s}{v_s}, \tag{3}$$

where ρ is the background mantle density at a given depth from the PREM model [*Dziewonski and Anderson*, 1981], and c is the conversion factor. This study uses three global tomographic models: SAW642ANb [*Panning et al*., 2010], S40RTS [*Ritsema et al*., 2011], and Smean [*Becker and Boschi*, 2002]. Each seismic model is divided into 20 shells with the identical thickness of 143.5 km, and $\frac{\delta v_s}{v_s}$ is interpolated at the middle depth of each shell with one-degree-by-one-degree grids. Following the previous studies [e.g., *Hager and Richards*, 1989], we ignore the structure in the top ~280 km of the mantle where large seismic anomalies are significantly affected by compositional or/and anisotropic effects but may not affect the long-wavelength geoid.

The geoid is computed by φ/g, where φ is the surface gravitational potential anomaly and can be solved from the Poisson's equation,

$$\nabla^2\varphi=-4\pi G\delta\rho, \tag{4}$$

where G is the gravitational constant, and $\delta\rho$ includes both density variations in the mantle ($\delta\rho$ in equation (3)) and those associated with dynamic topographies at the surface and CMB. Dynamic topographies are determined from solving equations (1) and (2) under free-slip boundary conditions at the surface and CMB. The self-gravitation effect is incorporated in this study although the equations presented above did not include this effect for simplicity. With the self-gravitation effect, an additional term, $-\rho\delta g\vec{\boldsymbol{e}}_{\boldsymbol{r}}$, should be added to the left side of equation (2) where $\delta g=-\nabla\varphi$ is the perturbation to the radial gravity [e.g., *Zhong et al*., 2008]. A reduced pressure formulation is used here to solve the momentum equation, dynamic topographies, gravitational potential and geoid with the self-gravitation effect [e.g., *Zhang and Christensen*, 1993; *Zhong et al*., 2008].

The flow models in this study consider only radially varying viscosity structure, as to be discussed in details later. Consequently, the conservation equations can be solved with a propagator-matrix method [e.g., *Hager and Richards*, 1989]. Details in solving the conservation equations and the Poisson's equation for the geoid and dynamic topographies with the self-gravitation can be found in *Zhong et al*. [2008]. In this study the density contrasts at the surface and the CMB are assumed as 3300 kg/m^3 and 4337 kg/m^3, respectively.

The compensation effect revealed from *Liu and Zhong* [2015] suggests that the long-wavelength geoid is only contributed from the upper part of the mantle above the compensation layer, while the buoyancy structure in the compensation layer can be ignored. The compensation thickness as inferred from dynamically consistent thermochemical convection models [*Liu and Zhong*, 2015] varies at different spherical harmonic degrees, and at degree 2 it is estimated to be 2–3 times the thickness of chemical piles. In this study, we assume a uniform compensation thickness at all degrees in thermochemical models based on the estimation at degree 2. This assumption does not affect the overall geoid modeling, given that the geoid is predominantly at degree-2 and the compensation layer resides at the lowermost mantle which has a limited influence on the geoid at shorter wavelengths. The thickness or vertical extent of the LLSVPs is not well constrained, and in particular, there are significant vertical variations in seismic anomalies within the LLSVPs [e.g., *Wang and Wen*, 2004; *He and Wen*, 2009]. Therefore, a precise knowledge of the compensation thickness is unknown, and in our thermochemical mantle models we consider four possible compensation thicknesses of 430 km, 720 km, 1000 km, and 1500 km.

2.2. Constraining the Radial Viscosity Structure and the Conversion Factor

The instantaneous models use a 1-D, layered viscosity structure. This allows the use of a propagation matrix method to compute velocities, stresses, dynamic topographies and the geoid from kernels [e.g., *Hager and O'Connell*, 1981], making it possible for efficiently sampling model parameter space. The effects of lateral variations in mantle viscosity on the geoid at long-wavelengths (degrees 2–3) may be secondary to that of vertical variations in viscosity for the present-day mantle structure [*Zhang and Christensen*, 1993; *Moucha et al*., 2007; *Ghosh et al*., 2010; *Liu and Zhong*, 2015], although such effects depend on mantle structures [*Zhong and Davies*, 1999]. Geoid modeling studies have utilized various parameterizations for the radial viscosity [e.g., *Hager and Richards*, 1989; *Steinberger and Calderwood*, 2006]. With a concern of potential

tradeoffs, our models do not employ fine viscosity layering, but only include four viscosity layers that coincide with significant phase transitions and seismic velocity stratifications. The viscosities in the lithosphere (0–100 km depths), the upper mantle (100–410 km depths), the transition zone (410–670 km depths), and the lower mantle (below 670 km) are denoted as η_{lith}, η_{um}, η_{tz}, and η_{lm}, respectively. The geoid is only sensitive to relative viscosity changes between different layers but not to the absolute viscosity [e.g., *Hager and Richards*, 1989]. Since the lithospheric viscosity has a weak impact on the long-wavelength geoid compared with that of mantle viscosities [*Thoraval and Richards*, 1997], we fix η_{lith} as 20. Recognizing that when assuming an 1-D viscosity profile as in this study that cannot include weak plate margins, a weak lithosphere is required in the geoid modeling [e.g., *Zhong and Davies*, 1999; *Ghosh et al*., 2010], we treat η_{um}, η_{tz}, and η_{lm} as free parameters while requiring that η_{lm} is larger than η_{lith}, i.e., η_{lm} is larger than 20.

The conversion factor c in equation (3) can be inferred from mineral physics studies [e.g., *Karato*, 1993] as well as modeling surface observables [e.g., *Forte and Mitrovica*, 2001]. In this study, c is taken as a constant in the whole mantle except for the compensation layer in which c is zero, and c is treated as the fourth free parameter in our model calculation in addition to the three viscosities.

We have computed the geoid and dynamic topography in a large number of models in which these four free parameters are varied. These four parameters are constrained by fitting the model geoid to the observation. For each group of these four parameters, the model geoid, denoted as H', is computed up to degrees and orders 12, and the fit to the observed geoid, H, is measured by the variance reduction [e.g., *Ricard et al*., 1993]:

$$V_{2-12}=1-\frac{M_{2-12}}{H_{2-12}}, \tag{5}$$

where H_{2-12} is the total power of the observed geoid H from degrees 2 to 12 and is computed by

$$H_{2-12}=\sum_{l=2}^{12}\sum_{m=0}^{l}\left[\left(H_{cos}^{lm}\right)^2+\left(H_{sin}^{lm}\right)^2\right]. \tag{6}$$

M_{2-12} in equation (5) is the total power of the difference between the model geoid H' and the observed geoid H from degrees 2 to 12:

$$M_{2-12}=\sum_{l=2}^{12}\sum_{m=0}^{l}\left[\left(H'^{lm}_{cos}-H_{cos}^{lm}\right)^2+\left(H'^{lm}_{sin}-H_{sin}^{lm}\right)^2\right]. \tag{7}$$

The degree-correlation $C_{lmin\text{-}lmax}$ between the model and observed geoids is computed by

$$C_{lmin-lmax}=\left[\sum_{l=lmin}^{lmax}\sum_{m=0}^{l}\left(H'^{lm}_{cos}H_{cos}^{lm}+H'^{lm}_{sin}H_{sin}^{lm}\right)\right]/\left(H'_{lmin-lmax}H_{lmin-lmax}\right)^{\frac{1}{2}}, \tag{8}$$

where $H'_{lmin-lmax}$ and $H_{lmin-lmax}$ are the total power of the model and observed geoids, respectively, from degrees *lmin* to *lmax*, and are computed by equation (6). Degree-correlation reveals the similarity between the patterns of the model and observed geoids at certain wavelengths.

In our geoid modeling calculations, these four free parameters, i.e., η_{um}, η_{tz}, η_{lm}, and the conversion parameter c, are firstly searched in a large parameter space with relatively coarse parameter grids. Guided by the fitting to the observed geoid, i.e., the variance reduction V_{2-12}, the search space is then narrowed down with refined parameter grids to the parameter space for models with large variance reductions, as to be discussed later.

3. Results

3.1. Results of the Geoid Models and Inverted Viscosities

3.1.1. Models With Restriction $\eta_{tz} \geq \eta_{um}$

Following *Hager and Richards* [1989], our study starts from models with a strong transition zone, i.e., $\eta_{tz} \geq \eta_{um}$ is preconstrained in the geoid modeling. The original search space is η_{um} between 0.01 and 10, η_{tz} between 0.1 and 20, and η_{lm} between 1 and 100, respectively. Ten different values with equal spacing in a logarithmic scale are searched for each viscosity parameter. Notice that we require that $\eta_{lm} \geq \eta_{tz} \geq \eta_{um}$. The

Table 1. The Best-Fit Geoid Models With Restriction $\eta_{tz} \geq \eta_{um}$[a]

		SAW642ANb				S40RTS				SMEAN			
		WM	TC1	TC2	TC3	WM	TC1	TC2	TC3	WM	TC1	TC2	TC3
V_{2-12} (%)		77.9	75.1	68.7	55.8	69.3	68.2	63.6	55.2	70.1	67.3	62.0	50.5
C	2–12	88.3	86.6	82.9	74.7	83.3	82.6	79.7	74.3	83.8	82.1	78.7	71.1
(%)	2	96.7	96.1	96.4	94.3	93.3	93.1	91.1	84.6	93.3	94.5	91.4	87.4
	3	92.7	94.3	93.8	92.4	90.3	90.5	91.2	92.9	84.9	83.7	84.8	81.9
η	*um*	0.7	0.5	0.7	0.6	0.6	0.5	0.4	0.5	0.5	0.4	0.6	0.5
	tz	0.7	0.5	0.7	0.6	0.6	0.5	0.4	0.5	0.5	0.4	0.6	0.5
	lm	40	30	35	30	35	30	25	25	35	30	35	30
c		0.28	0.32	0.36	0.4	0.26	0.28	0.32	0.38	0.24	0.28	0.32	0.36

[a]WM denotes whole mantle model, and TC1, TC2, and TC3 represent thermochemical models assuming a compensation thickness of 430 km, 720 km, and 1000 km, respectively. V_{2-12} is the degrees 2–12 variance reduction of the observed geoid. *C* is the degree-correlation with the observed geoid, 2–12 denotes the total correlation from degree 2 to degree 12, and 2 and 3 denote the correlation at degree 2 and degree 3, respectively. η is the radial viscosity, and *um*, *tz*, and *lm* denote the upper mantle, the transition zone, and the lower mantle, respectively. *c* is the conversion factor from seismic velocity to density anomaly.

conversion factor *c* is searched between 0.1 and 0.5 with a uniform spacing of 0.02. For each zoom-in procedure, the "best-fit" model with the largest variance reduction, $V_{2-12(max)}$, is identified, and models with variance reduction that is larger than $V_{2-12(max)}-5\%$ are considered as acceptable. Two seismic models, SAW642ANb and S40RTS, are used in the zoom-in procedure, and both the whole mantle convection and the thermochemical convection with a 720 km compensation thickness are assumed and tested. The parameter space of those acceptable models defines a starting search space for the next zoom-in procedure.

The zoom-in procedure is done twice, and the parameter space is narrowed down to be η_{um} between 0.1 and 1, η_{tz} between 0.1 and 2.5, and η_{lm} between 10 and 80, with refined intervals of 0.1, 0.1, and 5, respectively. The conversion factor *c* is between 0.22 and 0.34 for the whole mantle models, and 0.30–0.42 for the thermochemical models, both with an interval of 0.02. Thousands of models are computed within this parameter space, and their geoid outputs are analyzed. We mostly describe results based on seismic model SAW642ANb as it leads to slightly better geoid fits, but the results including the inverted parameters and the analyses shown in the following sections for S40RTS and Smean are quite similar (Tables 1 and 2).

For the whole mantle models, the largest variance reduction V_{2-12} is 78%, and in this best-fit model (Figure 2a), η_{um}, η_{tz}, η_{lm}, and *c* are 0.7, 0.7, 40, and 0.28, respectively. For all the models with $V_{2-12} > 73\%$, η_{tz} is mostly equal to or slightly larger than η_{um}, and the viscosity ratio between the lower mantle and the upper mantle is 40–200. Similar viscosity profiles are inferred from the thermochemical models, but a larger conversion factor is needed for fitting the geoid. The largest variance reduction for thermochemical models with a 720 km compensation thickness (Figure 2b) is 69%, and η_{um}, η_{tz}, η_{lm}, and *c* for this model are 0.7, 0.7, 35, and 0.36, respectively. Viscosity profiles for models with V_{2-12} larger than 64% is illustrated in Figure 3a. The variance reduction for thermochemical models is generally smaller than that of whole mantle models, and decreases with increasing compensation thickness (Table 1).

Table 2. The Best-Fit Geoid Models Without Restriction $\eta_{tz} \geq \eta_{um}$[a]

		SAW642ANb					S40RTS				SMEAN			
		WM	TC1	TC2	TC3	TC4	WM	TC1	TC2	TC3	WM	TC1	TC2	TC3
V_{2-12} (%)		83.4	81.3	76.6	64.8	32.8	80.0	80.1	77.3	70.0	80.8	79.7	77.0	69.2
C	2–12	91.3	90.2	87.6	80.5	57.3	89.5	89.5	87.9	83.9	89.9	89.3	87.7	83.7
(%)	2	98.7	98.4	98.2	95.1	53.6	96.2	96	93.8	88.8	97.0	96.4	94.6	90.4
	3	94.5	95.5	95.7	93.7	83.8	93.2	93.6	94.4	95.1	89.3	90.3	91.1	91.3
η	*um*	7	6.5	7	6	7	6	5	6	2	10	9	4	5
	tz	0.45	0.45	0.5	0.5	0.5	0.1	0.08	0.08	0.06	0.15	0.15	0.1	0.1
	lm	50	45	45	40	45	30	25	25	15	45	40	25	25
c		0.32	0.36	0.42	0.5	0.4	0.3	0.36	0.42	0.48	0.3	0.36	0.42	0.48

[a]TC4 represent thermochemical models assuming a compensation thickness of 1500 km. Other symbols and notations are same with those in Table 1.

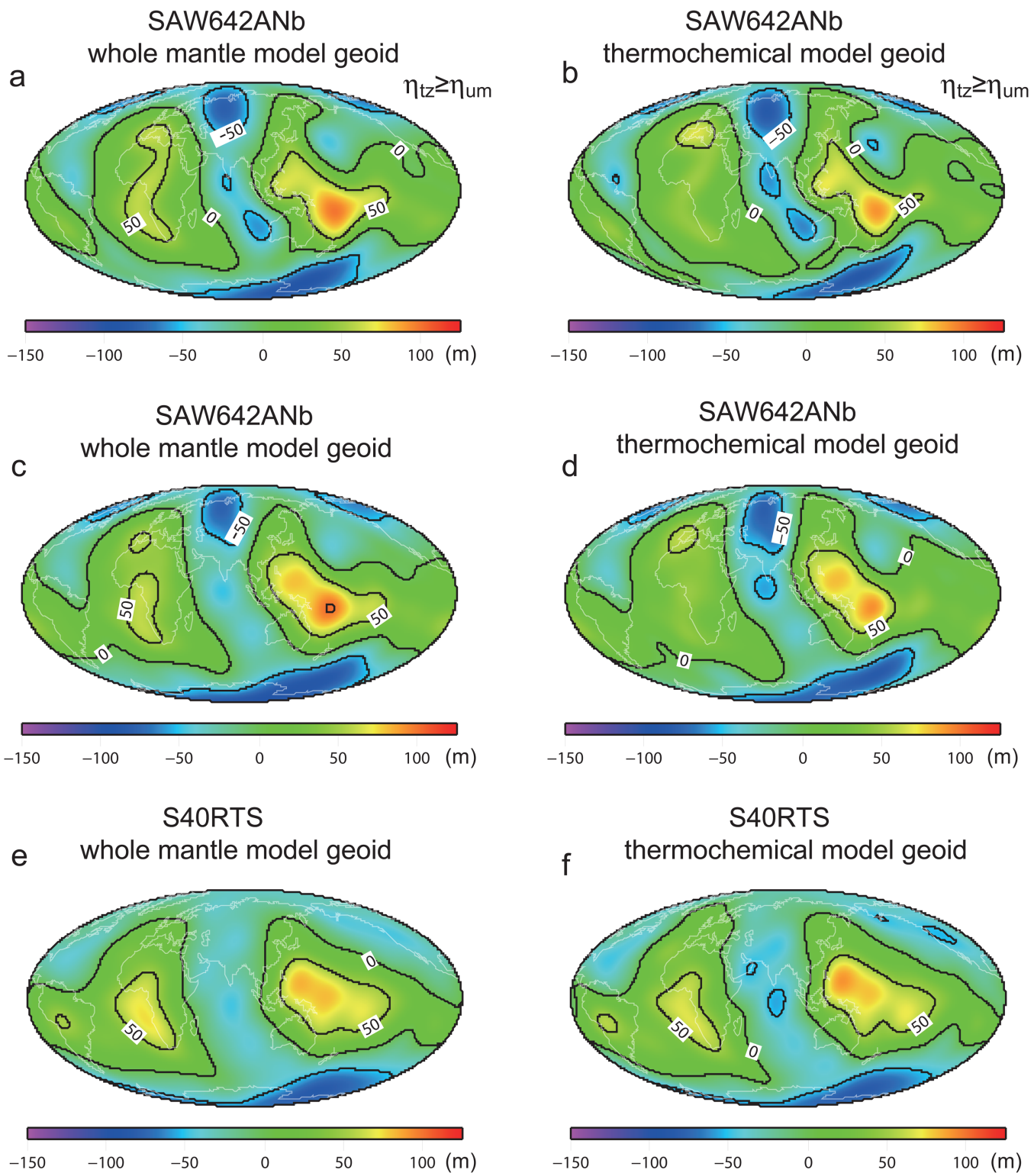

Figure 2. The best-fit model geoids computed up to degrees and orders 12 using seismic models (a–d) SAW642ANb, and (e, f) S40RTS. Figures 2a, 2c, and 2e are for whole mantle convection models, and Figures 2b, 2d, and 2f are for thermochemical convection models with a 720 km thick compensation layer. Figures 2a and 2b are for models with restriction $\eta_{tz} \geq \eta_{um}$, while Figures 2c–2f do not have the restriction. Contours of 50 m are plotted in (a)–(f).

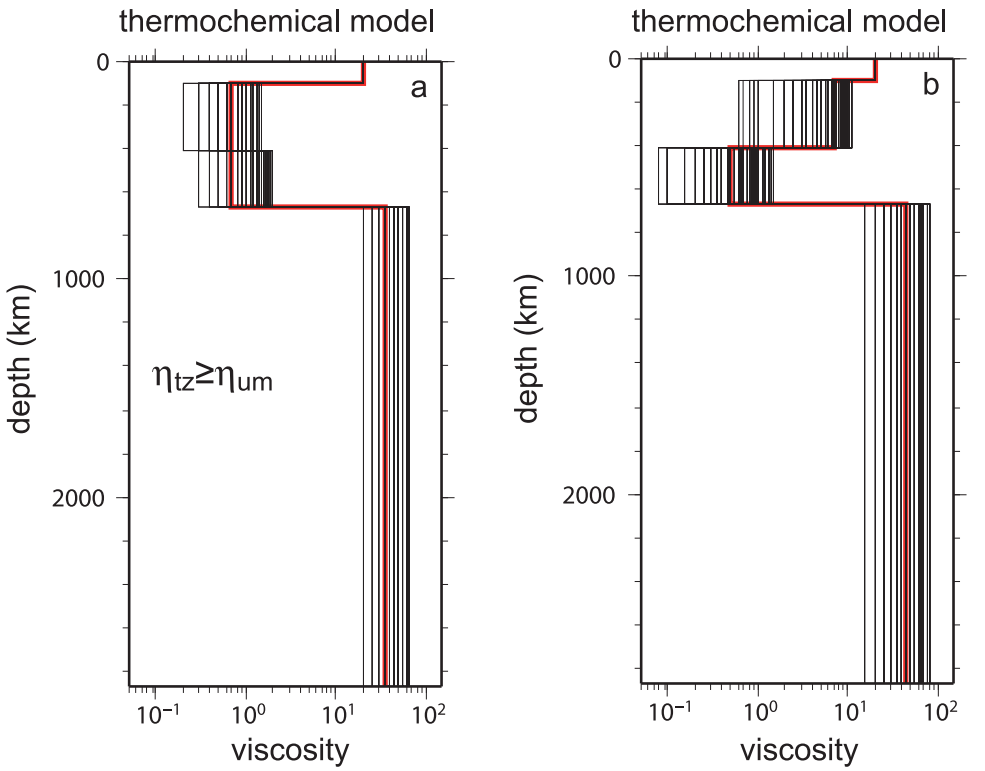

Figure 3. Viscosity profiles of thermochemical convection models with a 720 km thick compensation layer. (a) Models with restriction $\eta_{tz} \geq \eta_{um}$ that has a variance reduction larger than 64%, and (b) models without restriction $\eta_{tz} \geq \eta_{um}$ that has a variance reduction larger than 74%. Red lines denote the best-fit models.

Our inverted viscosity contrast η_{lm}/η_{um}~50 is quite similar to that inferred from geoid studies assuming a single viscosity layer for the upper mantle and transition zone (i.e., $\eta_{tz}=\eta_{um}$) [e.g., *Hager et al*., 1985]. However, with the $\eta_{tz} \geq \eta_{um}$ restriction in the inversion, the fact that in models with a large variance reduction η_{tz} is equal or close to η_{um} (Figure 3a) suggests that a weak transition zone, i.e., $\eta_{tz}<\eta_{um}$, needs to be considered. Therefore, we conduct an inversion without the restriction between η_{tz} and η_{um}.

3.1.2. Models Without Restriction $\eta_{tz} \geq \eta_{um}$

Without restriction on η_{tz} and η_{um}, the original search space is same as that employed in the section 3.1.1, except that the space for η_{tz} is expanded as from 0.01 to 20. The zoom-in procedure is done twice, and the final guided search space is 0.1–12 for η_{um}, 0.02–1.5 for η_{tz}, and 10–80 for η_{lm}. The interval for η_{um} is 0.1 between 0.1 and 1, and 0.5 between 1 and 12, respectively, the interval for η_{tz} is 0.02 between 0.02 and 0.1, and 0.05 between 0.1 and 1.5, respectively, and the interval for η_{lm} is uniformly 5. Assuming the whole mantle convection, the best-fit model (Figure 2c) has a variance reduction V_{2-12} of 83% (Table 2), with mantle viscosities of 7, 0.45, and 50 for the upper mantle, the transition zone, and the lower mantle, respectively, and a conversion factor of 0.32. Notice that all the models with V_{2-12} larger than 78% have a weaker transition zone than the upper mantle. The degree-correlations with the observed geoid at degrees 2 and 3 for the best-fit geoid, C_2 and C_3, are 99% and 95%, respectively, implying a nearly perfect reproduction of the long wavelength geoid.

For whole mantle convection models, we identified a large number of models with different viscosity structures that lead to similarly good variance reduction. For models with a very large variance reduction ($V_{2-12} > 80\%$), the viscosities for the upper mantle, η_{um}, and transition zone, η_{tz}, range from 0.5 to 11, and 0.1 to 1.2, respectively, and the lower mantle viscosity η_{lm} is between 20 and 80. For those models, viscosity ratios, η_{lm}/η_{um} and η_{tz}/η_{um}, range from 0.02 to 0.45, and 4.5 to 42, respectively. Viscosity ratios for models with a large variance reduction show a consistent trend and η_{tz}/η_{um} varies proportionally with η_{lm}/η_{um} (Figure 4a). The viscosity contrast at the 670 km depth, η_{lm}/η_{tz}, for these models with a large variance reduction falls in a narrow range between 60 and 250. Most of the acceptable models have c=0.32.

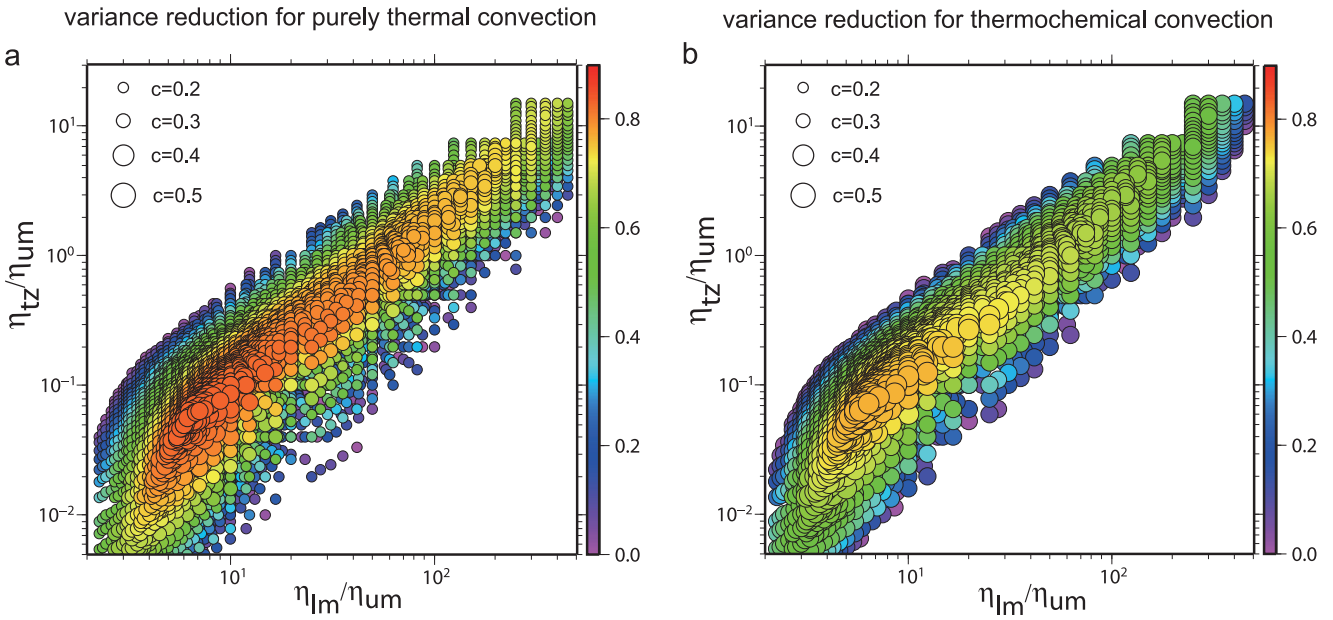

Figure 4. The variance reduction of the geoid in the logarithmic scale for (a) the whole mantle model and (b) the thermochemical model assuming a 720 km thick compensation layer, based on the seismic model SAW642ANb. Horizontal and vertical axes are the viscosity ratios of the lower mantle over the upper mantle and of the transition zone over the upper mantle, respectively. The color and size of the circles indicate the variance reduction and the conversion factor, respectively. In Figures 4a and 4b, for each radial viscosity profile, only the model with a conversion factor that best reproduces the observed geoid is plotted.

The inversion is performed for thermochemical models considering the compensation effect. Calculations are done with different compensation thicknesses of 430 km, 720 km, 1000 km, and 1500 km. Except for models with a 1500 km thick compensation layer, thermochemical models reproduces the observed geoid well (Figure 2d). For models with a 720 km thick compensation layer, the variance reduction V_{2-12} for the best-fit model is 77% (Table 2). V_{2-12} for the best-fit model decreases with increasing compensation layer thickness (Table 2), similar to calculations with restriction $\eta_{tz} \geq \eta_{um}$. For a 1500 km thick compensation layer, the best variance reduction V_{2-12} is only 33% (Table 2), suggesting that the compensation layer cannot be too thick. The viscosity profiles for the best-fit models (Table 2) are almost indistinguishable from those for the whole mantle convection. The tradeoffs for the inversion parameters are also analyzed, and for models with relatively large variance reduction, both the viscosity parameters and their ratios fall in very similar ranges to those for the whole mantle convection model (Figures 4a and 4b). The conversion factor for models with $V_{2-12}>72\%$ ranges from 0.38 to 0.44, and the best-fit model has c=0.42.

Without the restriction $\eta_{tz} \geq \eta_{um}$, the geoid constrains that the transition zone is weaker than the upper mantle (Figure 3b), and the geoid fit is significantly improved compared with models with that restriction in the section 3.1.1 (Tables 1 and 2). In the following sections, the analyses are focused on these models with a weak transition zone.

3.2. Power Spectrum and Degree-Correlation of the Model Geoid Contributed From Different Depths

The Earth's geoid is prevalently at long wavelengths [*Lerch et al.*, 1983, Figure 1b]. The power (equation (6)) of the geoid at degrees 2 and 3 accounts for 65% and 21%, respectively, of the total power from degrees 2 to 12 (Figure 10d). The long wavelength components of the geoid have a deep source [*Hager and Richards*, 1989], and are highly correlated with the lower mantle structure such as LLSVPs (Figure 1a). Section 3.1 shows that after removing the mantle buoyancy structure in the bottom ~1000 km thick compensation layer as expected for the thermochemical mantle model, those instantaneous models can still reproduce the geoid with a similar viscosity structure to that in whole mantle convection models. It is of interest where the long wavelength geoid (i.e., degrees 2 and 3) in those thermochemical models is originated from, and how the contributions from different depths vary between the two types of mantle models.

For the best-fit model assuming the whole mantle convection, the geoid contributed from each depth is dominantly at degree-2 across the mantle except for depths of ~1000–1300 km (Figure 5a). Between the

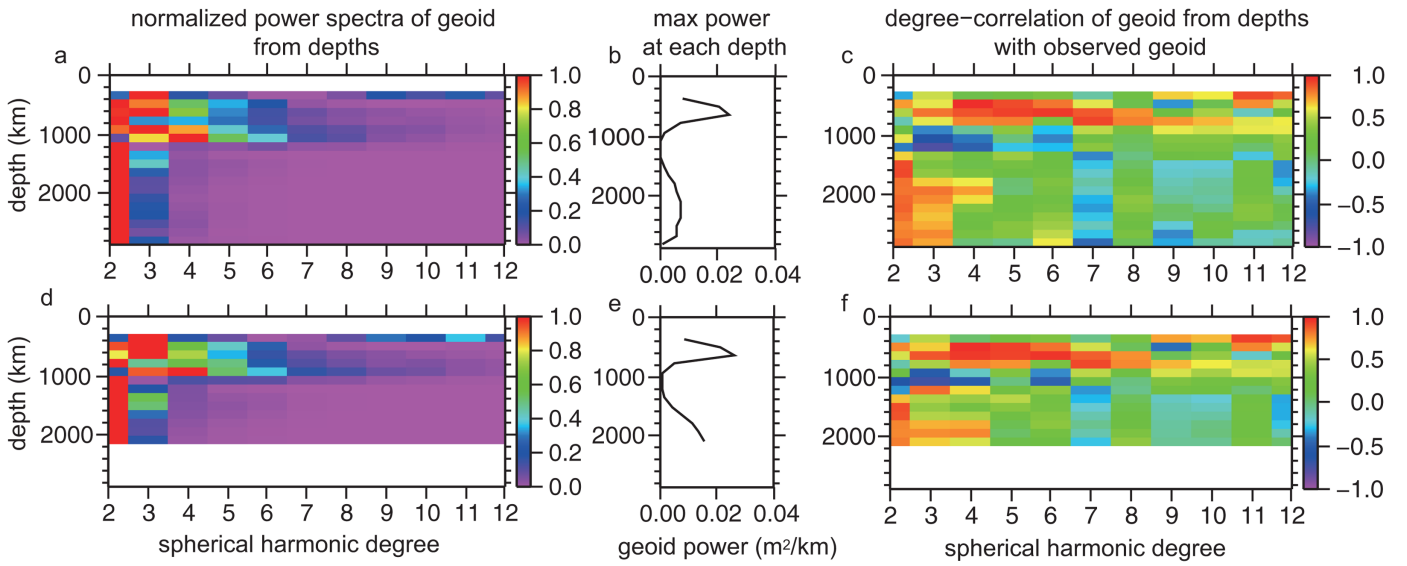

Figure 5. (a) The normalized power spectra of the geoid at degrees 2–12 contributed from different depths, (b) the maximum power among degrees 2–12 contributed from the layer with unit thickness at each depth, that is used to normalize the power spectra in Figure 5a at the corresponding depth, and (c) the degree-correlation between the observed geoid and the geoid contributed from a given depth for the whole mantle convection model. (d–f) Counterparts of Figures 5a–5c, respectively, for the thermochemical convection model with a 720 km thick compensation layer. (a)–(f) are for the best-fit geoid models using the seimic model SAW642ANb.

depths of 1000–1300 km the geoid power is relatively small (Figure 5b), and this is mainly because the geoid is insensitive to the buoyancy at these depths where the geoid kernels at long wavelengths (e.g., degree 2) are near 0 (Figure 6a). In the top 1000 km of the mantle, although the geoid power at degree 2 from each depth is large with a maximum at ~600 km depth (Figure 5b), the effective contribution from this region to the observed geoid is limited due to the poor degree-correlation at long wavelengths (Figure 5c). In total, the square root power of the degree 2 geoid contributed from this region is ~ 56 m, with a degree-correlation of 47% with the observed geoid. In contrast, at degree 2, the geoid contributed from below the 1300 km depth, with a total square root power of 96 m, is highly correlated (80%) with the observed geoid. It can be concluded that the degree 2 observed geoid is mainly originated from the lower mantle below the 1300 km depth. Analyses are also done on the degree 3 geoid. Although the geoid from the deep mantle (i.e., below the 1300 km depth) has a very large correlation at degree 3 (Figure 5c), the power is too small compared to that from the upper part of the mantle (Figures 5a and 5b). As a result, the lower and upper parts of the mantle have similar effective contributions to the observed geoid at degree 3. At degree 3, the geoid contributed from the lower mantle below the 1300 km depth has a square root power of 35 m, and a degree-correlation of 70%, while the geoid from the upper region (above the 1000 km depth) has a square root power of 45 m, and a degree-correlation of 79% with the observed geoid. At shorter wavelengths, the geoid is largely originated from the mantle above ~1000 km depth (Figure 5a).

Analyses are performed for the best-fit model assuming the thermochemical convection with a compensation thickness of 720 km. The difference of the viscosity profiles between this model and the whole mantle model is minimal (Table 2). The power spectra and the degree-correlation of the geoid from difference depths (Figures 5d–5f) share similar patterns to that of the whole mantle model (Figures 5a–5c). The geoid power from ~1000 km to ~1300 km is nearly zero. At degree 2, the geoid power reaches maximum both at ~600 km depth in the upper mantle and at the depth above the compensation layer, but the degree-correlation is much higher in the lower mantle (Figure 5f). The square root power of the degree 2 geoid from below the ~1300 km depth is ~74 m, with a degree-correlation of 80% with the observed geoid, while the mantle above the 1000 km depth contributes a square root power of 49 m with a degree-correlation of 50% with the degree 2 observed geoid. Therefore, the degree 2 geoid is mainly originated from the lower part of the mantle, similar to the whole mantle model as discussed earlier.

It is noticed that even after removing mantle structure in the bottom 720 km thick layer, the geoid power contributed from below 1300 km depth in the thermochemical model is still comparable to that in the

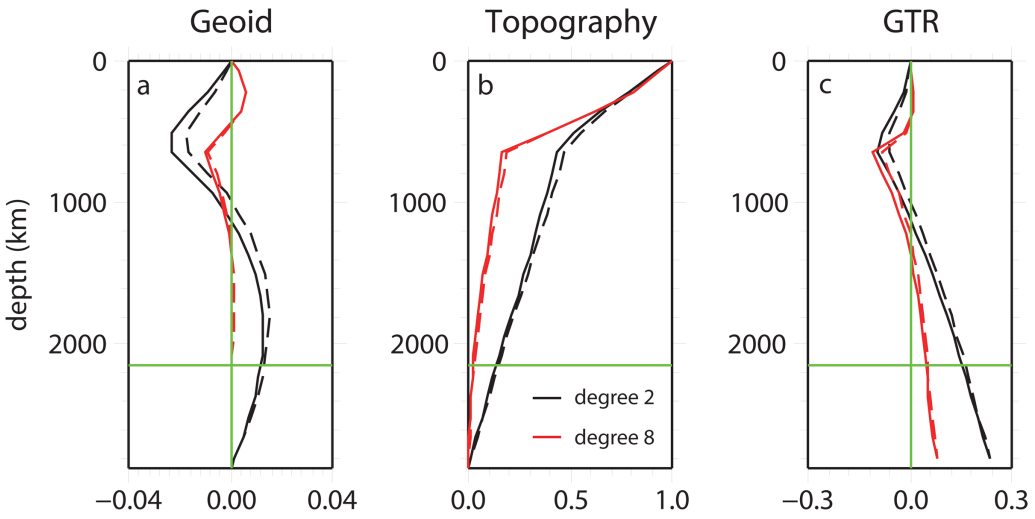

Figure 6. Kernels of (a) geoid, (b) surface dynamic topography, and (c) GTR for the best-fit models assuming both the whole mantle convection (solid lines) and the thermochemical convection with a 720 km thick compensation layer (dashed lines) at degrees 2 (black) and 8 (red). The vertical and horizontal green lines mark the value of 0 and the compensation depth, respectively.

whole mantle model (Figures 5b and 5e). Notice that Figure 5c also represents the degree-correlation between the seismic structure and the observed geoid. The seismic structure, hence the buoyancy structure, is continuous from the lowermost mantle to the midmantle, and is highly correlated with the observed geoid below the 1300 km depth. The slight difference in the viscosity profile between the whole mantle and thermochemical models causes a noticeable difference in the geoid kernels at degree 2 (Figure 6a). In the lower mantle below the 1300 km depth, the positive geoid kernel is larger in the thermochemical model than that in the whole mantle model. Since the buoyancy structure at midmantle depths is highly correlated with the observed geoid, the larger geoid kernel, together with an increase of the conversion factor *c*, make it possible for the thermochemical model to fit the degree-2 geoid using mantle buoyancy between the 1300 km depth and the compensation layer.

3.3. Surface Dynamic Topography and Geoid-to-Topography Ratio (GTR)

Surface dynamic topographies are computed for the best-fit models assuming the whole mantle convection and the thermochemical convection with a 720 km thick compensation layer (Figures 7a and 7b) by convolving topography kernels (Figure 6b) with mantle buoyancy. Surface dynamic topography in the thermochemical model shows similar patterns to that in the whole mantle model, but with larger amplitudes, particularly at relatively short wavelengths (Figures 7a and 7b). This can be understood from the topography kernels and the geoid-to-topography ratio (GTR).

For both thermochemical and whole mantle models, topography kernels are positive across the mantle, and are nearly identical. Notice that when assuming the thermochemical convection, the buoyancy structure in the compensation layer is removed, and would not contribute to the topography. However, the thermochemical model requires a larger conversion factor compared with that of the whole mantle convection to explain the geoid, implying that the mantle structure above the compensation layer would result in larger buoyancy and produce larger surface dynamic topography. At relatively short wavelengths (e.g., degree 8), the topography kernels for both models are negligibly small at depths of the compensation layer (Figure 6b). Consequently, in both models, the relatively short wavelength topography is mainly generated by the buoyancy structure in the upper part of the mantle above the compensation depth. Therefore, the thermochemical model with a larger conversion factor *c* would have a larger topography at these wavelengths compared with that of the whole mantle model. The ratio of the relatively short-wavelength topographies between the two models is approximately the ratio of their conversion factor *c* with the topography of the thermochemical model being ∼30% larger (Figure 7c).

At long wavelengths (e.g., degree 2), the buoyancy in the compensation layer makes a noneligible contribution to the surface topography in the whole mantle model (Figure 6b). For the thermochemical mantle

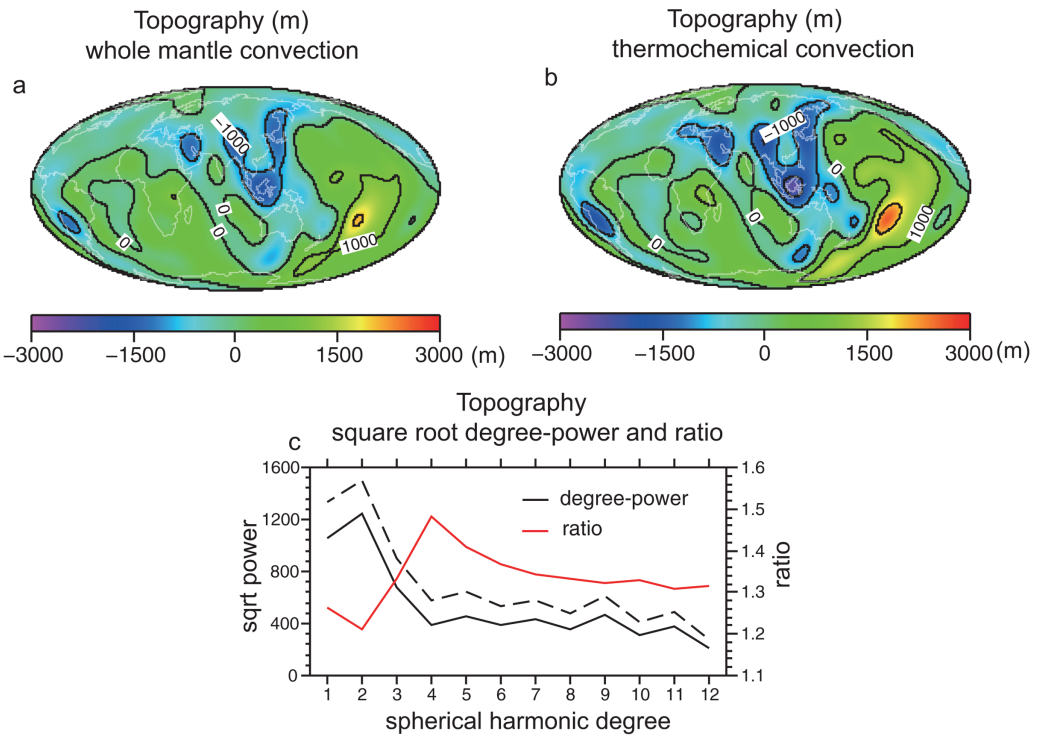

Figure 7. The surface dynamic topography for the best-fit models based on SAW642ANb assuming (a) the whole mantle convection, and (b) the thermochemical convection with a 720 km thick compensation layer. Contour lines of 1000 m are plotted in Figures 7a and 7b. (c) The square root degree-power of Figure 7a (solid line) and Figure 7b (dashed line), and the ratio of Figure 7b over Figure 7a (red line).

model, the effect of a larger conversion factor on the topography is partially offset by the effect of removing the buoyancy in the compensation layer. However, the dynamic topography in the thermochemical model would still be larger than that in the whole mantle model, although the difference between these two models is smaller than that at relatively short-wavelengths (Figure 7c), and that is because in the lower mantle below ~1200 km depth, the geoid-to-topography ratio (GTR) at degree 2 for both models are positive and increase with depth. Removing the buoyancy in the compensation layer in the thermochemical model would result in a reduced averaged GTR compared with that of the whole mantle model. A smaller GTR implies that, to produce the same observed geoid, the thermochemical model would produce more topography.

4. Discussion

4.1. The Geoid, Thermochemical Mantle Convection, and Structure in the Lower Mantle

Our study shows that the long-wavelength geoid anomalies can be reproduced in thermochemical mantle models in which the LLSVPs are interpreted as stable, negatively buoyant chemical piles. Therefore, our study helps resolve the dilemma that while the geoid observation appears to support isochemical, whole-mantle model [e.g., *Hager and Richards*, 1989; *Forte and Mitrovica*, 2001], seismic and geochemical observations require that the mantle has large-scale, stable chemical heterogeneities including the LLSVPs [e.g., *Jackson et al*., 2014; *Boyet and Carlson*, 2005]. In modeling the geoid from seismic models for a thermochemical mantle, our study considers the compensation effect of stable, negatively buoyant chemical piles on the geoid [*Liu and Zhong*, 2015] that helps circumvent difficulties in inferring the buoyancy for thermochemical heterogeneities such as the LLSVPs in seismic models.

In the whole mantle convection model, the deep mantle with the LLSVPs plays a critical role in explaining the long wavelength geoid. However, the thermochemical model in our study reproduces the observed geoid, although a significant part of the lower mantle above CMB (i.e., a compensation layer of ~1000 km thick) is removed due to the compensation effect. That the thermochemical model fits the geoid well without the structure in the bottom ~1000 km thick layer of the mantle is rather surprising, given that the

degree-2 buoyancy structure in this layer including the LLSVPs contributes significantly to the geoid in the whole mantle model (Figure 5b). The good geoid fitting arises because the degree-2 mantle seismic and hence buoyancy structure is continuous from CMB to the midmantle depth (~1300 km depth), and is highly correlated with the observed geoid. The buoyancy structure in the midmantle effectively contributes to the long wavelength geoid and makes it possible for thermochemical models to reproduce the observed geoid (Figures 5d–5f), without the buoyancy structure in the compensation layer, as shown in section 3.2.

Our results have a number of implications for mineral physics and seismology. First, notice that our thermochemical models considering the compensation effect suggest a larger conversion factor from seismic velocity to density anomalies in the isochemical part of the mantle above the compensation layer. This should have implications for mantle mineral physics. Second, our thermochemical models indicate an important role of mantle structure in the midmantle above the compensation layer in explaining the geoid. However, seismic tomographic models often do not have as good resolution at this depth range as that for the bottom of the mantle. Therefore, future seismic studies should seek to further improve the resolution at the midmantle depths. Third, our thermochemical models suggest that the vertical extent of chemically dense and stable piles (i.e., LLSVPs) above the CMB may not exceed 300–500 km. Seismic estimates of vertical extent of chemically distinct LLSVPs or superplumes range from several hundreds to over a thousand kilometers, based on the anti-correlation of shear wave and bulk sound speeds [*Masters et al*., 2000] or wave-form modeling [*Ni et al*., 2002; *Wen et al*., 2001; *He and Wen*, 2009]. *Ni et al*. [2002] suggested that the African anomaly, where compositional anomalies are embedded in thermal plumes, would rise to as high as ~1000 km from the CMB. However, it is unclear how thick the chemically dense and stable portion of LLSVPs is. Our results show that thermochemical models with a compensation layer thinner than 720 km reproduce the observed geoid well, while the geoid fitting decreases rapidly with thicker compensation layer, especially with layers thicker than 1000 km (e.g., the variance reduction decreases from 77% to 65% as the compensation layer thickness increases from 720 to 1000 km, respectively, and it drops to 33% as the layer thickness increases to 1500 km) (Table 2), indicating an upper bound of compensation layer thickness of ~1000 km. Considering that, from studies of mantle convection models [*Liu and Zhong*, 2015], the compensation layer thickness is about twice of the vertical extent of chemically dense piles with uniform density, our results suggest an upper bound of the vertical extent of chemically dense piles of ~ 300–500 km above the CMB. This is consistent with seismic studies of anti-correlation between shear velocities and bulk sound velocities in LLSVPs [*Masters et al*., 2000]. However, this does not necessarily contradict with the existence of chemically distinct superplume structure rising to shallower depths as suggested in *Ni et al*. [2002], if such a structure is not negatively buoyant. For example, *Tan and Gurnis* [2005] proposed a compressible thermochemical convection model where metastable superplumes are dynamically maintained while negatively buoyant materials only exist in the upper part of thermochemical piles. We think that the geoid modeling such as that done in *Liu and Zhong* [2015] could provide an important test for these models.

4.2. A Weak Transition Zone

An important outcome of the geoid modeling is to place constraints on mantle viscosity structure [e.g., *Hager and Richards*, 1989]. Our study with the whole mantle and thermochemical mantle models reveals two important features about mantle viscosity. First, mantle viscosity inferred from the geoid in the thermochemical mantle model is nearly identical to that in the whole mantle model, suggesting that the viscosity inferred from previous whole mantle models [e.g., *Hager and Richards*, 1989] remains largely valid. Second, with three seismic models considered here (i.e., SAW642ANb, S40RTS and Smean), our study suggests that the transition zone appears to be the weakest, being ~10 times weaker than the upper mantle and ~100 times weaker than the lower mantle (Table 2), irrespective of the whole-mantle or the thermochemical mantle models.

Our result that the transition zone is significantly weaker than the upper mantle is different from *Hager and Richards* [1989] where a stronger transition zone is preferred. We suspect that the difference may be caused by the difference in the mantle buoyancy used in our studies. *King* [1995] found two groups of viscosity profiles, with either a strong or a weak transition zone that would reproduce the observed geoid. He suggested that a large viscosity contrast between the upper mantle and transition zone would be critical in the geoid modeling. Our study using most recent seismic models seems to remove the ambiguity in preferring a weaker transition zone. That the transition zone is significantly weaker than the upper mantle has implications for mineral physics. Compared with the upper mantle, the transition zone minerals have much higher

water solubility [e.g., *Williams and Hemley*, 2001; *Nestola and Smyth*, 2015], and the transition zone is estimated to have a water content of 0.2–2 wt% [*Bercovici and Karato*, 2003]. The high water content would weaken the transition zone, and provide a supporting observation for the inferred viscosity profile from our study.

It should be pointed out that if the transition zone is restricted not to be weaker than the upper mantle, i.e., $\eta_{tz} \geq \eta_{um}$, our modeling indicates that η_{tz} would be about the same as η_{um} which is ~50 times smaller than the lower mantle (Table 1) for both whole-mantle and thermochemical models. This result is consistent with those inferred for the whole-mantle model in previous studies [e.g., *Hager*, 1984; *Hager et al*., 1985; *Ricard et al*., 1993]. Previous studies also found that an extremely weak and thin layer around ~670 km depth would help fit the geoid [e.g., *Panasyuk and Hager*, 1998; *Forte et al*., 1993]. We do not attempt to divide the mantle into more viscosity layers to further resolve finer viscosity structure, due to our concern on computational costs and potential tradeoffs among a large number of viscosity layers, as seen in viscosity inversions using postglacial rebound observations [*Paulson et al*., 2007; *Paulson and Richards*, 2009].

4.3. Viscosity Structure in the Lower Mantle

While our models assume a constant lower mantle viscosity, previous studies on modeling gravitational anomalies or the postglacial rebound have employed viscosity models with significant viscosity increases within the lower mantle [e.g., *Steinberger and Calderwood*, 2006; *Forte and Mitrovica*, 2001]. Recently, using a Bayesian inversion procedure, *Rudolph et al*. [2015] suggested a viscosity increase at ~ 1000 km depth using geoid modeling for whole mantle convection models.

Following same procedure as described in sections 2 and 3 and assuming the whole mantle convection, we tested the robustness of the viscosity stratification at 1000 km depth. We employ a four-layer 1-D viscosity profile with contrasts at 100 km, 670 km, and 1000 km depths (the four viscosities are denoted as η_{lith}, η_{um}, η_{up-lm}, η_{bot-lm}, from the surface to the CMB, respectively), with a fixed η_{lith} of 20 as before, and a presumption that $\eta_{bot-lm} \geq \eta_{up-lm} \geq \eta_{um}$ (i.e., the viscosity monotonically increases with depth). Notice that we now combine the upper mantle and transition zone into one layer as the upper mantle for simplicity and reducing tradeoffs. After several zoom-in procedures, large amounts of models are calculated with η_{um}, η_{up-lm}, and η_{bot-lm} ranging from 0.02 to 7, 1 to 120, and 7 to 400, respectively. The best-fit model (V_{2-12}=77.90%) has a viscosity profile of η_{um}=0.4, η_{bot-lm}=30, and η_{up-lm}=30, respectively. Notice that no viscosity increase exists for this model at 1000 km depth. The model with the second large variance reduction (V_{2-12}=77.86%), however, has a viscosity jump at 1000 km from η_{up-lm}=8 to η_{bot-lm}=35, while its η_{um} is 0.6 which is close to that of the best-fit model. It is found that all the models that well reproduce the observed geoid (V_{2-12}>73%) have viscosity increase at 1000 km depth by a factor of 1 (i.e., no increase) to 10 (Figure 8). This significant tradeoff implies that a viscosity increase at 1000 km depth is not required from our geoid modeling study. The viscosity ratio of the upper mantle to the bottom lower mantle (i.e., below 1000 km depth), η_{um}/η_{bot-lm}, however, falls in a very narrow range of 1/30 to 1/100 (Figure 8), indicating that this

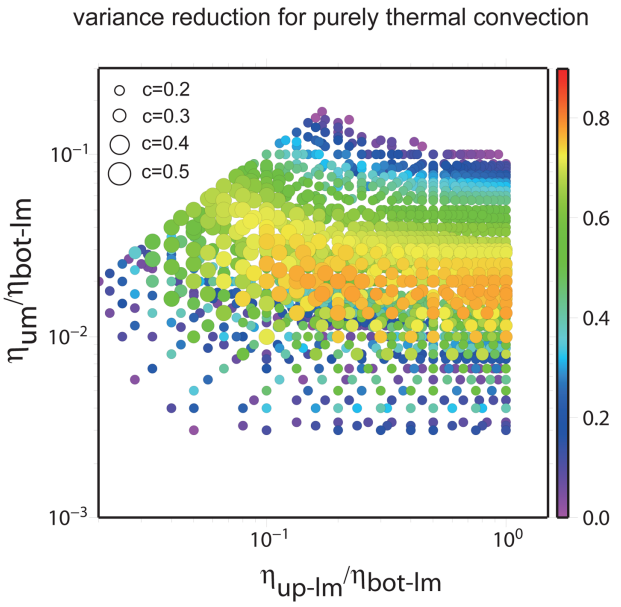

Figure 8. The variance reduction of the geoid in the logarithmic scale for whole mantle models with a presumed viscosity stratification at 1000 km depth, based on the seismic model SAW642ANb. Horizontal and vertical axes are the viscosity ratios of the upper part of the lower mantle (from 670 to 1000 km depths) to the bottom part of the lower mantle (below 1000 km depth), and of the upper mantle (from 100 to 670 km depths) to the bottom part of the lower mantle, respectively. The color and size of the circles illustrate the variance reduction and the conversion factor, respectively. For each radial viscosity profile, only the model with a conversion factor that best reproduces the observed geoid is plotted.

viscosity contrast is a rather robust inference from our geoid modeling. This result is also consistent with our results in section 3.1.1 and classic studies where the viscosity in the lower mantle is about 30–60 times that of the upper mantle [e.g., *Hager and Richards*, 1989]. The viscosity inversion with the same viscosity parameterization is also done for thermochemical models with a 720 km thick compensation layer. With viscosity structures similar with those inverted from whole mantle geoid models, thermochemical models can reproduce the observed geoid, although with smaller variance reductions. Thus, the compensation effect from thermochemical models does not affect the inferred viscosity stratification at 1000 km.

Therefore, our geoid modeling suggests that a more robust feature in the inferred mantle viscosity is a general increase of a factor of 30–100 from the upper mantle to the lower mantle, while it is not well constrained how and where the viscosity increases with the depth. A viscosity increase at ~1000 km depth as suggested by *Rudolph et al*. [2015] is possible but not required. Constraints other than the geoid observation are needed to better understand the fine-layered viscosity structure in the lower mantle. One of the main justifications for the viscosity contrast at ~1000 km depth proposed by *Rudolph et al*. [2015] is the seismic imaging of plumes and slabs that appear to change their morphologies at that depth [*Fukao et al*., 2009; *French and Romanowicz*, 2014]. However, more slab stagnations have been observed at the 670 km depth [e.g., *Fukao et al*., 2009]. If the same reasoning is followed, the slab stagnations at ~670 km depth would also suggest a viscosity increase there. Moreover, slab geometries involve complex mechanism. For example, slab stagnations may be heavily influenced by trench roll back [e.g., *Zhong and Gurnis*, 1995; *Christensen*, 1996] and subduction history [e.g., *Billen*, 2008]. More seismic and geodynamic studies are in need to further explore the slab structure and dynamics.

4.4. Dynamic Topography

Dynamic topography for the Earth may be estimated by removing the isostatic compensation effect on the topography and determining the residual topography [e.g., *Davies and Pribac*, 1993; *Lithogow-Bertelloni and Silver*, 1998; *Panasyuk and Hager*, 2000]. The residual topography can be estimated more robustly in oceanic regions than in continental regions because of the expected small variations in oceanic crustal structure. In oceanic regions, the residual topography shows topographic highs in central Pacific (i.e., the Pacific superswell) ranging from ~1 to 2 km depending on different lithospheric thermal models [*Panasyuk and Hager*, 2000]. Even after removing the effects of seamounts and oceanic islands, sediments, and the lithospheric thermal structure (i.e., the plate model), the central Pacific region still has ~1 km of residual topography [*Zhong et al*., 2007]. Over large length-scale ($>$ 6000 km or up to spherical harmonic degree 6), the estimated residual topography is generally in a range of $\sim\pm$1 km [e.g., *Panasyuk and Hager*, 2000].

In our best-fit geoid model assuming the whole mantle convection, the dynamic topography at degrees 2 and 3 (i.e., long-wavelength) are in the range of $\sim\pm$800 m and $\sim\pm$400 m, respectively, with a topographic high of ~1 km in the central Pacific. The dynamic topography from our geoid models is consistent with the estimated residual topography [*Panasyuk and Hager*, 2000] and the dynamic topography computed from other geoid modeling studies [e.g., *Hager and Richards*, 1989; *Lithogow-Bertelloni and Silver*, 1998]. It is of interest why the magnitude of the long wavelength dynamic topography is as high as ~1 km. While a recent study based on gravity-topography admittance argument suggested that dynamic topography may not exceed ~300 m at relatively small length-scales [*Molnar et al*., 2015], the admittance, or the geoid to topography ratio (GTR), may provide some insight for the high magnitude of the long wavelength topography in our model. Notice that the degree 2 GTR changes sign at ~1200 km depth, being negative above and positive below the depth (Figure 6c). The negative GTR reflects the negative geoid kernel in the upper mantle (Figure 6a), as the topography kernel is positive for the whole mantle (Figure 6b). The degree-2 seismic structure is a continuous feature from the upper to lower mantles (i.e., seismically slow below Africa and the central Pacific, Figures 9a and 9b). This suggests that dynamic topography produced by mantle structure at different depths generally adds to each other and highly correlates with the total surface topography (Figures 9e, 9f, and 9h). However, the degree-2 geoid from the upper mantle is largely canceled out by that from the lower mantle due to the opposite signs of the kernel in the two regions (Figures 9c and 9d). The overall GTR should be the average of the GTR kernel over the whole mantle, weighted by depth distribution of the power (e.g., Figure 5b). In our best-fit whole mantle geoid model, the degree 2 GTR kernel ranges from $-$0.15 at ~600 km depth to ~0.25 above the CMB, and an averaged GTR of less than 0.1 is expected. This explains why to produce the observed degree-2 geoid of ~70 m in the Pacific, the models

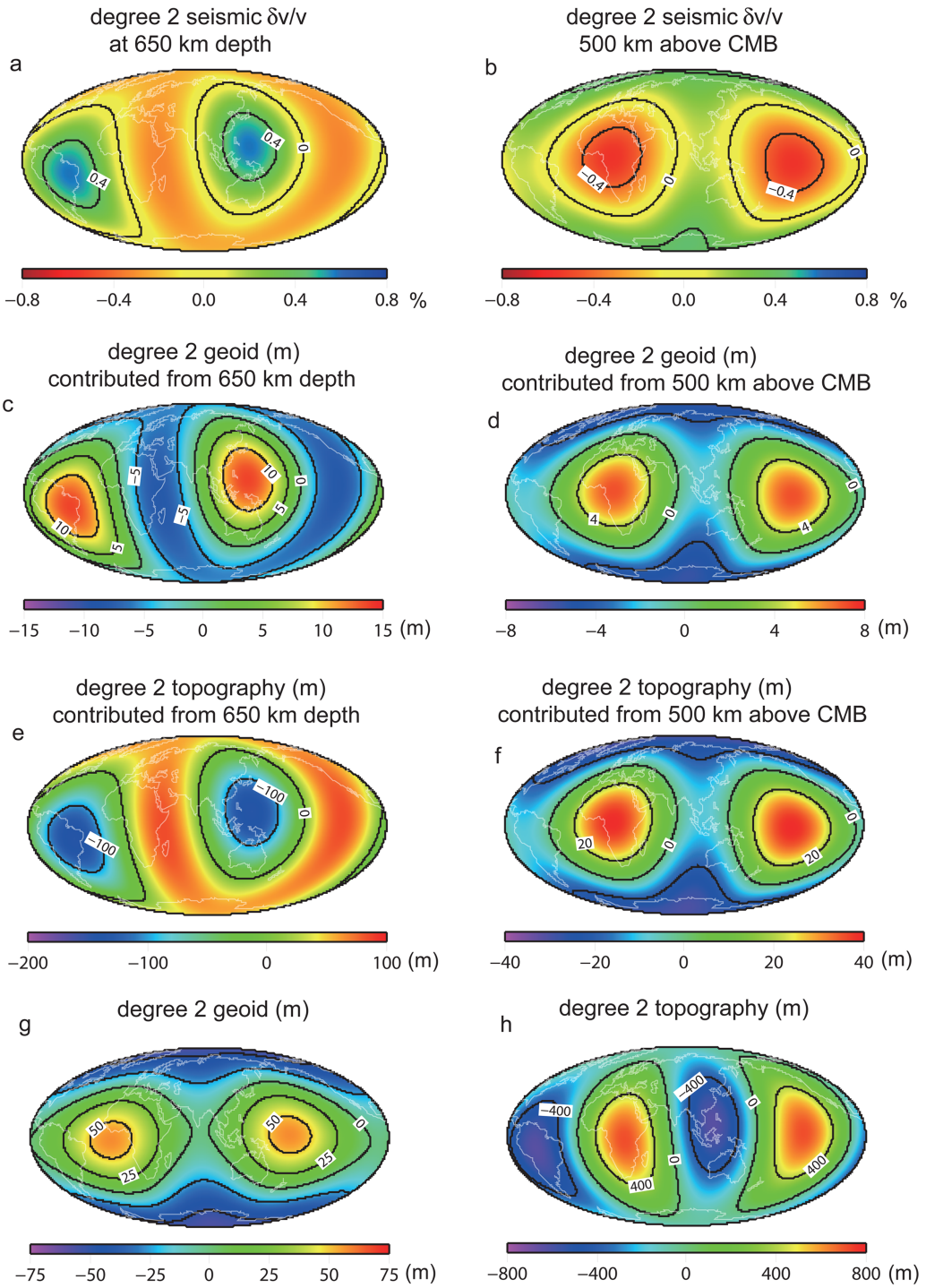

Figure 9. Seismic shear wave speed anomaly $\delta v/v$ (model SAW642ANb) at (a) 650 km depth and (b) 500 km above CMB. Degree 2 geoid contributed from (c) 650 km depth and (d) 500 km above CMB, degree 2 surface dynamic topography contributed from (e) 650 km depth and (f) 500 km above CMB, and total degree 2 (g) geoid and (h) surface dynamic topography, of the best-fit geoid model assuming the whole mantle convection based on model SAW642ANb.

often produce $\sim$ 800 m degree 2 topographic high there. The argument also applies for thermochemical mantle models, with an even smaller overall GTR.

While our whole mantle models for the geoid yield similar dynamic topography to that from previous studies, our thermochemical models with the compensation effect lead to larger amplitude of dynamic

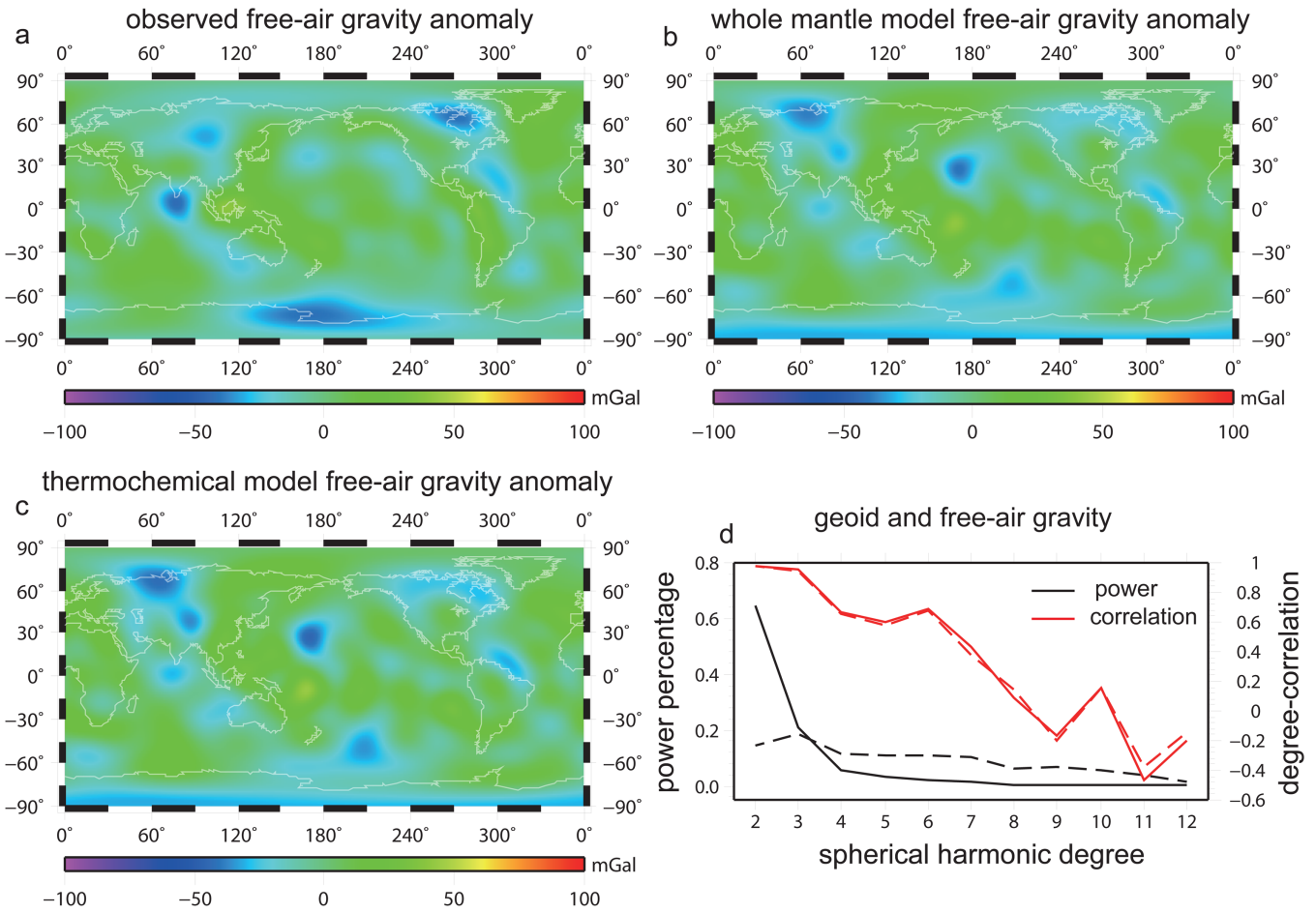

Figure 10. (a) Observed free-air gravity anomaly (model EGM2008), and computed free-air gravity anomalies for best-fit models assuming (b) the whole mantle convection, and (c) the thermochemical convection with a 720 km thick compensation layer. (d) Degree power percentages over degrees 2–12 (black) for the observed geoid (solid line) and free-air gravity (dashed line), and the degree-correlations (red) of the computed geoid (solid line) and free-air gravity (dashed line) with the observations for the best-fit thermochemical models with a 720 km thick compensation layer.

topography due to a larger conversion factor, compared with those for the whole mantle model. The difference, however, is not significant (<30% overall), and we suspect that it would be challenging to use the inferred residual topography to distinguish the whole mantle and the thermochemical mantle models. It should be noticed that, in thermochemical models, since the buoyancy structure in the lowermost mantle is removed, the model CMB topography cannot be used to make meaningful geophysical inference for which fully dynamic models are needed.

4.5. The Free-Air Gravity Anomaly

While the long wavelength structure in the Earth's gravitational field is well represented in the geoid (Figure 1b), the small-scale features are more evident in the free-air gravity anomalies (Figure 10a, EGM2008 model) [*Pavlis et al.*, 2013]. Notice that we have subtracted the free-air gravity anomaly caused by the glacial isostatic adjustment process [*Geruo et al.*, 2013] from the original EGM2008 model. The degree power for the geoid decreases rapidly as the wavelength decreases, while the free-air gravity anomalies have relatively flat power spectra (Figure 10d). This is because free-air gravity anomalies, gFA_{lm}, can be simply related to the geoid h_{lm} by $gFA_{lm}=(l-1)h_{lm}g/R$ where l is the spherical harmonic degree, g is the reference gravitational acceleration, and R is the Earth's radius.

We have computed *gFA* up to degrees and orders 12 for best-fit geoid models assuming both the whole mantle convection (Figure 10b) and the thermochemical convection with the compensation thickness of 720 km (Figure 10c), using the similar kernel approach. Both whole mantle and thermochemical models reproduce the long wavelength pattern of the *gFA* (Figures 10b and 10c). However, the model *gFA* has

significantly lower total degree-correlations with the observation with $C_{2\text{-}12}$ at 58% for the whole mantle model, and 52% for the thermochemical model, compared with the model geoid (e.g., Table 2). This is consistent with the findings from previous studies [e.g., *Forte et al*., 2008]. A close examination reveals that the degree-correlation is very high at degrees 2 and 3, and it decreases with harmonic degree. At relatively short wavelengths, the correlation is poor, and is smaller than 50% for degrees larger than 6 for both models (Figure 10d). It is also found that at each degree the correlation for *gFA* between the model and the observation is nearly identical to that for the geoid (Figure 10d). Since the geoid is dominantly at degrees 2 and 3, its total correlation as well as the variance reduction can be high even with poor degree-correlations at short wavelengths (Figure 10d).

The difference in spectral correlations for the geoid and free-air gravity anomalies may have implications for inference of mantle viscosity structure using these observations. For example, the inferred mantle viscosity from the geoid weighs more on long-wavelength mantle structure at the large depths, while free-air gravity based inference may incorporate more small-scale structure at relatively shallow depths. The small-scale structure at shallow depths may be more difficult to resolve seismically and interpret geodynamically due to uncertainties associated with anisotropy and compositional heterogeneities. Consequently, it is important to investigate optimal inversion procedures for mantle viscosity using these observations.

4.6. Potential Drawback and Future Work

In this study, the compensation effect of negatively buoyant chemical piles observed in dynamically self-consistent thermochemical convection models [*Liu and Zhong*, 2015] is utilized in the geoid modeling. This approach avoids the difficulty of determining the buoyancy structure of the chemical piles from the seismic structure. However, there are several potential drawbacks in this approach. While the dynamically self-consistent thermochemical models suggest that the compensation layer thickness is ~2–3 times of the chemical piles [*Liu and Zhong*, 2015], a precise knowledge on the compensation thickness for the Earth is unclear. Since the bottom part of the mantle is removed to account for the compensation effect, the CMB topography in our thermochemical models does not reveal the lower mantle dynamics that would be heavily influenced by the thermochemical piles. Our geoid modeling employs an 1-D viscosity, while the low viscosity of the chemical piles due to temperature and compositional effects might be important in the lower mantle dynamics. Nevertheless, the 1-D viscosity inverted from this study has laid a foundation for future studies to formulate instantaneous models based on seismic mantle structure with realistic temperature- and composition-dependent viscosity, and explore the buoyancy structure in the thermochemical piles and the ambient mantle by fitting the geoid and surface and CMB topographies.

5. Conclusion

In this study, we formulate instantaneous mantle flow models for the geoid and dynamic topography assuming both thermochemical and whole mantle convection with mantle buoyancy structure derived from seismic tomographic models SAWANb642, S40RTS, and Smean. Our models employ an 1-D viscosity structure and the geoid is calculated using the propagator matrix method. The thermochemical mantle model considers the compensation effect of the stable, negatively buoyant thermochemical piles (i.e., LLSVPs).

Our thermochemical mantle models treating the LLSVPs as negatively buoyant thermochemical piles can well reproduce the Earth's geoid, thus reconciling the geoid observation with the interpretation of the LLSVPs as long-term stable chemical reservoirs. The inferred mantle viscosity structure in the thermochemical model is nearly identical to that for the whole mantle model. Both models prefer a weak transition zone, and in the preferred viscosity model, the lower mantle viscosity is ~10 times higher than the upper mantle viscosity that is ~10 times higher than the transition zone viscosity. A larger conversion factor from seismic velocity to density anomalies is required to fit the geoid in the thermochemical mantle model compared with that of the whole mantle model, resulting in a larger (~30%) surface dynamic topography in the thermochemical model. The amplitude of long-wavelength (degrees 2 and 3) dynamic topography is about ±1.2 km, which is generally consistent with previous whole mantle models. Our geoid modeling studies suggest that the compensation layer is likely to be thinner than ~1000 km, and that the upper bound of the vertical extent of the chemically distinct and negatively buoyant piles or LLSVPs above the CMB is ~300–500 km. Our studies indicate that mantle structure at midmantle depths (e.g., between 1300 km and

2100 km depths) controls the geoid for a thermochemical mantle model. This suggests that future seismic models need to further improve resolution at the midmantle depths. While it is possible that the lower mantle viscosity may increase significantly with depth (e.g., at ~1000 km depth), the geoid modeling only provides a limited depth resolution, and a more robust conclusion is a general increase in viscosity by a factor of ~100 from the upper mantle to depths below 1000 km.

Acknowledgments
This work was funded by the National Science Foundation through grant 1135382. The authors wish to thank Editor-in-Chief Thorsten Becker, Scott King, and an anonymous reviewer for constructive reviews. Per the AGU Data Policy, all data required to reproduce the results described herein are available from the corresponding author upon request.

References

Becker, T. W., and L. Boschi (2002), A comparison of tomographic and geodynamic mantle models, *Geochem. Geophys. Geosyst.*, *3*(1), 1003, doi:10.1029/2001GC000168.
Bercovici, D., and S. Karato (2003), Whole-mantle convection and the transition-zone water filter, *Nature*, *425*, 39–44, doi:10.1038/nature01918.
Billen, M. I. (2008), Modeling the dynamics of subducting slabs, *Annu. Rev. Earth Planet. Sci.*, *36*, 325–356, doi:10.1146/annurev.earth36.031207.124129.
Boyet, M., and R. W. Carlson (2005), 142Nd evidence for early (> 4.53 Ga) global differentiation of the silicate Earth, *Science*, *309*, 576–581.
Christensen, U. R. (1996), The influence of trench migration on slab penetration into the lower mantle, *Earth Planet. Sci. Lett.*, *140*, 27–39.
Davaille, A. (1999), Simultaneous generation of hotspots and superswells by convection in a heterogenous planetary mantle, *Nature*, *402*, 756–760.
Davies, D. R., S. Goes, J. H. Davies, B. S. A. Schuberth, H.-P. Bunge, and J. Ritsema (2012), Reconciling dynamic and seismic models of Earth's lower mantle: The dominant role of thermal heterogeneity, *Earth Planet. Sci. Lett.*, *353*, 253–269, doi:10.1016/j.epsl.2012.08.016.
Davies, G. F., and F. Pribac (1993), Mesozoic seafloor subsidence and the Darwin Rise, past and present, in *The Mesozoic Pacific: Geology, Tectonics, and Volcanism*, vol. 77, edited by M. S. Pringle, AGU, Washington, D. C., doi:10.1029/GM077p0039.
Dziewonski, A. M., and D. L. Anderson (1981), Preliminary Reference Earth Model (PREM), *Phys. Earth Planet. Inter.*, *25*, 297–356.
Forte, A. M., and J. X. Mitrovica (2001), Deep-mantle high-viscosity flow and thermochemical structure inferred from seismic and geodynamic data, *Nature*, *410*, 1049–1056.
Forte, A. M., A. Dziewonski, and R. L. Woodward (1993), Aspherical structure of the mantle, tectonic plate motions, nonhydrostatic geoid, and topography of the core-mantle boundary, in *Dynamics of Earth's Deep Interior and Earth Rotation, Geophys. Monogr. 72*, edited by J.-L. Le Mouël, D. E. Smylie, and T. Herring, pp. 135–166, AGU, Washington, D. C.
Forte, A. M., S. Quéré, R. Moucha, N. A. Simmons, S. P. Grand, J. X. Mitrovica, and D. B. Rowley (2008), Joint seismic–geodynamic-mineral physical modelling of African geodynamics: A reconciliation of deep-mantle convection with surface geophysical constraints, *Earth Planet. Sci. Lett.*, *295*(3-4), 329–341, doi:10.1016/j.epsl.2010.03.017.
French, S., and B. Romanowicz (2014), Whole mantle radially anisotropic shear-velocity structure from spectral-element waveform tomography, *Geophys. J. Int.*, *199*, 1303–1327.
Fukao, Y., M. Obayashi, and T. Nakakuki (2009), Stagnant slab: A review, *Annu. Rev. Earth Planet. Sci.*, *37*, 19–46, doi:10.1146/annurev.earth.36.031207.124224.
Geruo, A., J. Wahr, and S. J. Zhong (2013), Computations of the viscoelastic response of a 3-D compressible Earth to surface loading: An application to glacial isostatic adjustment in Antarctica and Canada, *Geophys. J. Int.*, *192*, 557–572.
Ghosh, A., T. W. Becker, and S. J. Zhong (2010), Effects of lateral viscosity variations on the geoid, *Geophys. Res. Lett.*, *37*, L01301, doi:10.1029/2009GL040426.
Hager, B. H. (1984), Subducted slabs and the geoid: Constraints on mantle rheology and flow, *J. Geophys. Res.*, *89*, 6003–6015, doi:10.1029/JB089iB07p06003.
Hager, B. H., and R. O'Connell (1981), A simple global-model of plate dynamics and mantle convection, *J. Geophys. Res.*, *86*, 4843–4867.
Hager, B. H., and M. A. Richards (1989), Long-wavelength variations in Earth's geoid: Physical models and dynamical implications, *Philos. Trans. R. Soc. London A*, *328*, 309–327.
Hager, B. H., R. Clayton, M. A. Richards, R. Comer, and A. Dziewonski (1985), Lower mantle heterogeneity, dynamic topography and the geoid, *Nature*, *313*, 541–546, doi:10.1038/313541a0.
He, Y., and L. Wen (2009), Structural features and shear-velocity structure of the "Pacific Anomaly," *J. Geophys. Res.*, *114*, B02309, doi:10.1029/2008JB005814.
Hofmann, A. W. (1997), Mantle geochemistry: The message from oceanic volcanism, *Nature*, *385*, 219–229.
Jackson, M. G., S. R. Hart, J. G. Konter, M. D. Kurz, J. Blusztajn, and K. Farley (2014), Helium and lead isotopes reveal the geochemical geometry of the Samoan plume, *Nature*, *514*, 355–358.
Karato, S. (1993), Importance of anelasticity in the interpretation of seismic tomography, *Geophys. Res. Lett.*, *20*, 1623–1626.
Kellogg, L. H., B. H. Hager, and R. D. van der Hilst (1999), Compositional stratification in the deep mantle, *Science*, *283*, 1881–1884.
King, S. D. (1995), Radial models of mantle viscosity: Results from a genetic algorithm, *Geophys. J. Int.*, *122*, 725–734, doi:10.1111/j.1365-246X.1995.tb06831.x.
King, S. D., and G. Masters (1992), An inversion for radial viscosity structure using seismic tomography, *Geophys. Res. Lett.*, *19*, 1551–1554, doi:10.1029/92GL01700.
Kunz, J., T. Staudacher, and C. J. Allegre (1998), Plutonium-fission xenon found in Earth's mantle, *Science*, *280*, 877–880.
Lerch, F. J., S. M. Klosko, and G. B. Patel (1983), A refined gravity model from Lageos (GEML2), *NASA Tech. Memo. 84986*, Goddard Space Flight Cent., Greenbelt, Md.
Lithgow-Bertelloni, C., and P. G. Silver (1998), Dynamic topography, plate driving forces and the African superswell, *Nature*, *395*(6699), 269–272.
Liu, X., and S. J. Zhong (2015), The long-wavelength geoid from three-dimensional spherical models of thermal and thermochemical mantle convection, *J. Geophys. Res. Solid Earth*, *120*, 4572–4596. doi:10.1002/2015JB012016.
Masters, G., G. Laske, H. Bolton, and A. Dziewonski (2000), The relative behavior of shear velocity, bulk sound speed, and compressional velocity in the mantle: Implications for chemical and thermal structure, in *Earth's Deep Interior: Mineral Physics and Tomography From the Atomic to the Global Scale*, edited by S.-I. Karato et al., pp. 63–87, AGU, Washington, D. C.
McNamara, A. K., and S. J. Zhong (2005), Thermochemical structures beneath Africa and the Pacific Ocean, *Nature*, *437*, 1136–1139.
Mitrovica, J. X., and A. M. Forte (2004), A new inference of mantle viscosity based upon a joint inversion of convection and glacial isostatic adjustment data, *Earth Planet. Sci. Lett.*, *225*, 177–189.

Molnar, P., P. C. England, and C. H. Jones (2015), Mantle dynamics, isostasy, and the support of high terrain, *J. Geophys. Res. Solid Earth*, *120*, 1932–1957, doi:10.1002/2014JB011724.
Moucha, R., A. M. Forte, J. X. Mitrovica, and A. Daradich (2007), Lateral variations in mantle rheology: Implications for convection related surface observables and inferred viscosity models, *Geophys. J. Int.*, *169*, 113–135, doi:10.1111/j.1365-246X.2006.03225.x.
Nestola, F., and J. R. Smyth (2015), Diamonds and water in the deep Earth: New perspectives, *Int. Geol. Rev.*, *58*(3), pp. 263–276, doi:10.1080/00206814.2015.1056758.
Ni, S. D., E. Tan, M. Gurnis, and D. Helmberger (2002), Sharp sides to the African superplume, *Science*, *296*, 1850–1852.
Panasyuk, S. V., and B. H. Hager (1998), A model of transformational superplasticity in the upper mantle, *Geophys. J. Int.*, *133*(3), 741–755, doi:10.1046/j.1365-246X.1998.00539.x.
Panasyuk, S. V., and B. H. Hager (2000), Models of isostatic and dynamic topography, geoid anomalies, and their uncertainties, *J. Geophys. Res.*, *105*, 28,199–28,209.
Panning, M. P., V. Lekic, and B. A. Romanowicz (2010), The importance of crustal corrections in the development of a new global model of radial anisotropy, *J. Geophys. Res.*, *115*, B12325, doi:10.1029/2010JB007520.
Paulson, A., and M. A. Richards (2009), On the resolution of radial viscosity structure in modelling long-wavelength postglacial rebound, *Geophys. J. Int.*, *179*, 1516–1526, doi:10.1111/j.1365-246X.2009.04362.x.
Paulson, A., S. J. Zhong, and J. Wahr (2007), Limitations on the inversion for mantle viscosity from postglacial rebound, *Geophys. J. Int.*, *168*, 1195–1209, doi:10.1111/j.1365-246X.2006.03222.x.
Pavlis, N. K., S. A. Holmes, S. C. Kenyon, and J. K. Factor (2013), Correction to ''The Development and Evaluation of the Earth Gravitational Model 2008 (EGM2008)'', *J. Geophys. Res. Solid Earth*, *118*, 2633, doi:10.1002/jgrb.50167.
Ricard, Y., M. A. Richards, C. Lithgow-Bertelloni, and Y. Lestunff (1993), A geodynamic model of mantle density heterogeneity, *J. Geophys. Res.*, *98*, 21,895–21,909.
Ritsema, J., A. Deuss, H. J. van Heijst, and J. H. Woodhouse (2011), S40RTS: A degree-40 shear-velocity model for the mantle from New Rayleigh wave dispersion, teleseismic traveltime and normal-mode splitting function measurements, *Geophys. J. Int.*, *184*(3), 1223–1236, doi: 10.1111/j.1365-246X.2010.04884.x.
Rudolph, M. L., V. Lekić, and C. Lithgow-Bertelloni (2015), Viscosity jump in Earth's mid-mantle, *Science*, *350*(6266), 1349–1352, doi:10.1126/science.aad1929.
Steinberger, B., and A. R. Calderwood (2006), Models of large-scale viscous flow in the Earth's mantle with constraints from mineral physics and surface observations, *Geophys. J. Int.*, *167*, 1461–1481. doi:10.1111/j.1365-246X.2006.03131.x.
Steinberger, B., and T. H. Torsvik (2010), Toward an explanation for the present and past locations of the poles, *Geochem. Geophys. Geosyst.*, *11*, Q06W06, doi:10.1029/2009GC002889.
Su, W.J., and A. M. Dziewonski (1997), Simultaneous inversion for 3-D variations in shear and bulk velocity in the mantle, *Phys. Earth Planet. Inter.*, *100*, 135–156.
Tackley, P.J. (1998), Three-dimensional simulations of mantle convection with a thermochemical CMB boundary layer: D''?, in *The Core-Mantle Boundary Region, Geodyn. Ser.*, edited by M. Gurnis et al., pp. 231–253, AGU, Washington, D. C.
Tan, E., and M. Gurnis (2005), Metastable superplumes and mantle compressibility, *Geophys. Res. Lett.*, *32*, L20307, doi:10.1029/2005GL024190.
Thoraval, C., and M. A. Richards (1997), The geoid constraint in global geodynamics: Viscosity structure, mantle heterogeneity models and boundary conditions, *Geophys. J. Int.*, *131*, 1–8.
Wang, Y., and L. X. Wen (2004), Mapping the geometry and geographic distribution of a very low velocity province at the base of the Earth's mantle, *J. Geophys. Res.*, *109*, B10305, doi:10.1029/2003JB002674.
Wen, L. X., P. Silver, D. James, and R. Kuehnel (2001), Seismic evidence for a thermo-chemical boundary at the base of the Earth's mantle, *Earth Planet. Sci. Lett.*, *189*, 141–153.
Williams, Q., and R. Hemley (2001), Hydrogen in the deep earth, *Annu. Rev. Earth Planet. Sci.*, *29*, 365–418.
Zhang, N., S. J., Zhong, W. Leng, and Z. X. Li (2010), A model for the evolution of the Earth's mantle structure since the Early Paleozoic, *J. Geophys. Res.*, *115*, B06401, doi:10.1029/2009JB006896.
Zhang, S. X., and U. Christensen (1993), Some effects of lateral viscosity variations on geoid and surface velocities induced by density anomalies in the mantle, *Geophys. J. Int.*, *114*, 531–547.
Zhong, S. J., and G. F. Davies (1999), Effects of plate and slab viscosities on the geoid, *Earth Planet. Sci. Lett.*, *170*, 487–496, doi:10.1016/S0012-821X(99)00124-7.
Zhong, S. J., and M. Gurnis (1995), Mantle convection with plates and mobile, faulted plate margins, *Science*, *267*, 838–843.
Zhong, S. J., M. Ritzwoller, N. Shapiro, W. Landuyt, J. Huang, and P. Wessel (2007), Bathymetry of the Pacific Plate and its implications for thermal evolution of lithosphere and mantle dynamics, *J. Geophys. Res.*, *112*, B06412, doi:10.1029/2006JB004628.
Zhong, S. J, A. McNamara, E. Tan, L. Moresi, and M. Gurnis (2008), A benchmark study on mantle convection in a 3-D spherical shell using CitcomS, *Geochem. Geophys. Geosyst.*, *9*, Q10017, doi:10.1029/2008GC002048.